TÜBİTAK

Turkish Journal of Physics

http://journals.tubitak.gov.tr/physics/

Research Article

Turk J Phys
(2013) 37: 312 – 321

doi:10.3906/fiz-1303-4

Effect of microwave sintering on grain size and dielectric properties of barium titanate

Praveena KURUVA,[1,2,*] **Uma Maheshwara Singh RAJAPUTRA,**[2]
Srinath SANYADANAM,[3] **Ramana Murthy SARABU**[2]
[1]Materials Research Center, Indian Institute of Science, Bangalore, India
[2]Department of Physics, Osmania University, Hyderabad, India
[3]School of Physics, University of Hyderabad, Hyderabad, India

Received: 07.03.2013 • **Accepted:** 21.05.2013 • **Published Online:** 13.09.2013 • **Printed:** 07.10.2013

Abstract: In the present paper, nanosized barium titanate ($BaTiO_3$) powders were synthesized by microwave hydrothermal method. The structural characterization of as-prepared powders was investigated using X-ray diffraction and Fourier transform infrared spectroscopy. The particle size was estimated using a transmission electron microscope. The nanopowders were sintered at different temperatures using a microwave furnace, followed by characterizations such as X-ray diffraction and field emission scanning electron microscopy. The dielectric constant behavior was observed as a function of frequency (100 Hz to 1 MHz) and temperature. The ferroelectric nature was confirmed from polarization-electric field loops.

Key words: Ferroelectrics, microwave hydrothermal method, microwave sintering, dielectric properties, P-E loops

1. Introduction

Ferroelectric ceramics with perovskite structure like barium titanate ($BaTiO_3$) are extensively used in the electronics industry for the fabrication of multilayer ceramic capacitors, piezoelectric transducers, positive temperature coefficient resistors, and ferroelectric memories. For these applications, materials of high dielectric constants and low losses are required. The synthesis of barium titanate nanoparticles with controlled size and composition is of fundamental technological interest [1,2]. In the past decade, extensive studies have been conducted for synthesizing nanosized $BaTiO_3$ powders with narrow particle size distribution, controlled morphology, and high purity [3].

Powders prepared using different synthesis routes have problems due to chemical inhomogeneity and reactivity. In addition, it gives a wide range of grain sizes, and very little control is possible for the size, shape, and agglomeration of particles. Thus, alternate routes to synthesis based on novel low-temperature processes, like the microwave hydrothermal (M-H) method, are of significance to yield high-purity, ultrafine powders with controlled morphology and size of particles. Various low-temperature routes involving organometallic precursors like alkoxides, acetates, oxalates, nitrates, and citrates of Ba and Ti have been used in the past to obtain $BaTiO_3$ [4–6]. Apart from these methods, sol-gel [7], sol-precipitation [8], and hydrothermal [9] and organic polymeric precursor [10] routes have been used for the preparation of $BaTiO_3$ powders. In the present investigation, the nanopowders of $BaTiO_3$ were prepared using the M-H method. This technique exhibits better control over particle size, crystallinity, and dispersibility of synthesized $BaTiO_3$ nanoparticles.

*Correspondence: praveena@mrc.iisc.ernet.in

In the present work, we have done a systematic study of synthesis and the microwave sintering process at different temperatures, and of their characterization.

2. Experimental

The synthesis of nanosized $BaTiO_3$ powders was reported by the authors elsewhere [11]. The fundamentals of microwave heating were discussed in detail by Metaxas and Binner [12]. The as-prepared powders were characterized by X-ray diffraction (XRD), transmission electron microscope (TEM), and Fourier transform infrared (FTIR). XRD was carried out using a Philips (PANalytical) X-ray diffractometer with Cu-K_α radiation ($\lambda =$ 1.5406 Å) to characterize the as-prepared $BaTiO_3$ powders. The particle size and morphology were investigated using a TEM (Model JEM-2010, JEOL, Tokyo, Japan). FTIR spectra were recorded on a Bruker Tensor 27 spectrophotometer from 4000 cm^{-1} to 375 cm^{-1} using the KBr pellet method. Sintering is a process by which powder compacts are strengthened at elevated temperatures. It usually involves volume shrinkage and densification in reduction of porosity. The process of sintering is very often studied by measuring shrinkage or density of the materials. In the present investigation, $BaTiO_3$ was mixed with a 2 wt.% polyvinyl alcohol (binder) and pressed at a pressure of 6 MPa for 1 min into pellets (3 mm in length, 10 mm diameter) without any lubricant. The samples were sintered at different sintering temperatures of 800, 850, 900, and 950 °C/30 min using a microwave sintering method and were characterized using XRD and scanning electron microscope (SEM) (LEICA, S440i, UK). The SEM was operated at 10 kV to 20 kV of accelerating voltage with 10,000× magnification. The magnification was kept constant for all the samples for the sake of comparison. The confirmation of ferroelectric nature was made by studying polarization (P)-electric field (E) loop measurements. One consequence of the domain-wall switching in ferroelectric materials is the occurrence of the ferroelectric hysteresis loop. This study helps in understanding different physical processes that take place in ferroelectric materials, e.g., domain-wall pinning, defect ordering, and the nature of defects [13]. The P-E measurements were made at room temperature using a Sawyer-Tower circuit (radiant ferroelectric tester, RT-66A).The measurements were carried out on the samples whose thickness lay between 0.4 and 0.8 mm. The samples were kept in a sample holder, which was dipped in silanol oil, and an electric field was applied. From the hysteresis loops, the remanent polarization, which determines the charge retained by the sample, and the coercive field were estimated.

3. Results and discussion

3.1. Characterization

Figure 1 shows the X-ray powder diffraction patterns for $BaTiO_3$ powder. It is observed that the powders have a pure tetragonal phase confirmed from the (1 1 0) peak. The broad peaks in the XRD indicate the nano nature of samples. The impurity phase of $BaCO_3$ (at $2\theta \sim 34°$) in Figure 1 was not detected in the XRD pattern. The lattice constant of the ferroelectric phase was a = 4.000 Å and c = 4.012 Å.

The average particle size of the as-synthesized powders of $BaTiO_3$ was estimated from the X-ray line broadening of the (1 1 0) peak using the Scherer formula [14]:

$$D = \frac{0.9\lambda}{\beta Cos\theta},$$

where D is the average particle size, λ is the wavelength of X-rays used, and β is the width of the diffraction peak at half-maximum for the diffraction angle 2θ.

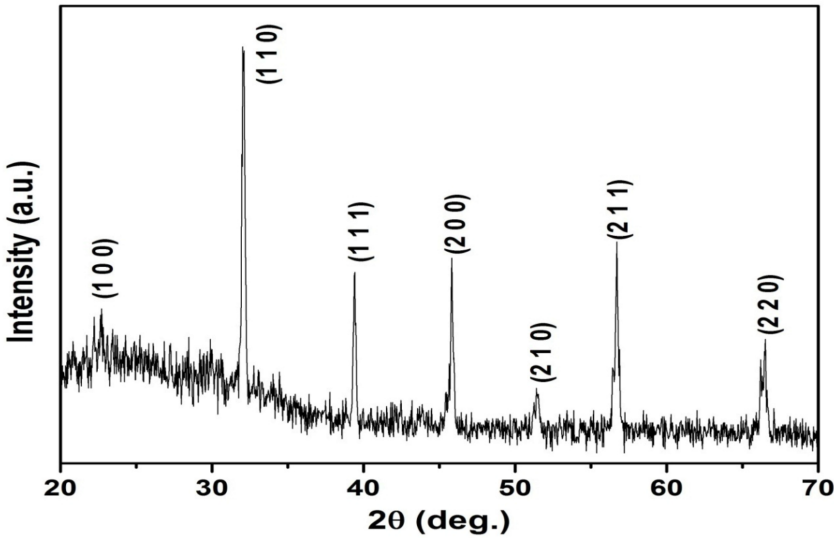

Figure 1. XRD pattern of as-synthesized $BaTiO_3$ powders.

The lattice constant (Å) for the present samples is calculated by using a given set of planes (h k l) and using the following equations.

For cubic crystals, d_{hkl} is given by:

$$d_{hkl} = \frac{a}{\sqrt{h^2 + k^2 + l^2}} \mathring{A}. \tag{1}$$

For tetragonal crystals, d_{hkl} is given by:

$$\frac{1}{d} = \sqrt{\frac{4}{3}\left(\frac{h^2 + k^2}{a^2}\right) + \frac{l^2}{c^2}} \mathring{A}^{-1}. \tag{2}$$

The Archimedes principle [8] was used to measure the bulk density (d_{bulk}) of all the prepared ferroelectric samples. The bulk density of the sample is given by

$$d_{bulk} = \frac{M_{air}}{M_{air} - M_{xylene}} d_{xylene} g/cm^3, \tag{3}$$

where M_{air} is mass of the sample in air and M_{xylene} is mass of the sample in xylene.

The X-ray position and the intensity maximum corresponding to each peak vary depending on the amount of ferroelectric phase. The X-ray density of individual phases was calculated from the values of the calculated lattice parameters using the following relation:

$$d_x = \frac{8M}{Na^3} g/cm^3, \tag{4}$$

where M is the molecular weight, N is the Avogadro number, and 'a' is the lattice constant. With the knowledge of X-ray density (d_x) and bulk density (d_{bulk}), the value of porosity for the samples is estimated using the following relation.

$$\text{Porosity } (P\%) = \left(1 - \frac{d_{bulk}}{d_x}\right) \times 100 \tag{5}$$

Figure 2 shows the TEM picture of the $BaTiO_3$ powders. It can be seen that the powder particles are well distributed and the size of the powders is $\sim$30 nm. These values are in agreement with those calculated from XRD peaks. It can also be seen from the selected area electron diffraction (SAED) photograph that particles possess uniform size and spherical morphology.

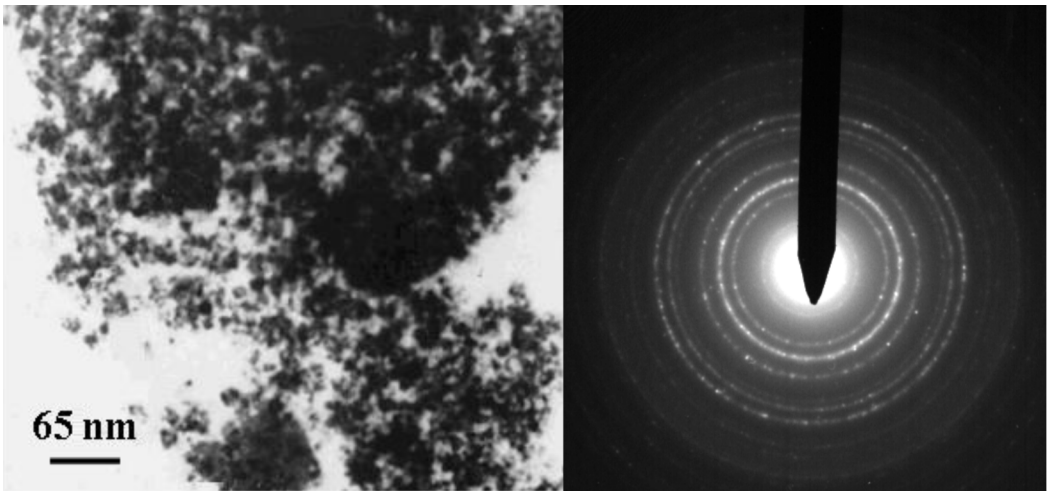

Figure 2. TEM and SAED pictures of $BaTiO_3$ powders.

3.2. FTIR analysis

Figure 3 shows the FTIR spectra of the as-synthesized $BaTiO_3$ powder. FTIR was found to be the most sensitive technique for the detection of $BaCO_3$ [15]. It can be observed from Figure 3 that the cubic $BaTiO_3$ powder has symmetry and hence it shows 2 absorption bands due to the Ti-$O_{\perp}$ stretching vibration along the polar (c) axis and the $O_{|}$-Ti-$O_{||}$ bending vibration of TiO_6 octahedra in the ranges of 640–480 and 480–375 cm^{-1}, respectively. Thus, the 2 bands with the center positions at $\sim$570 cm^{-1} and 420 cm^{-1} were found to be almost corresponding with the Ti-$O_{|}$ stretching vibration of the vertical and the $O_{|}$-Ti-$O_{||}$ bending vibration of the TiO_6 octahedron of the cubic $BaTiO_3$. The band at 850 cm^{-1} is ascribed to the antisymmetric stretching vibration of NO_3^{-1}, arising from the residual nitrate. The peak at $\sim$1440 cm^{-1} corresponds to the asymmetric stretch of the simple carbonate ion CO_3^{-2}.

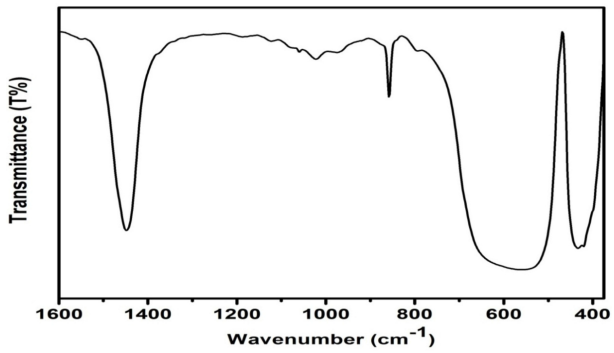

Figure 3. FTIR spectra of as-synthesized $BaTiO_3$ nanopowders.

Figure 4 shows the XRD patterns of $BaTiO_3$ sintered at different temperatures. All the peaks were indexed with JCPDS Card No.: 82-1175. No impurity phase was observed in the XRD. The values of lattice parameters, X-ray density, bulk density, and porosity are given in Table 1. It could be seen that as the sintering temperature increases, the lattice constants were increasing from 3.898 to 3.999 Å due to the unit cell expansion. The bulk densities of the samples were also increasing with temperature due to the fact that a rise in temperature results in grain growth, thereby decreasing the porosity.

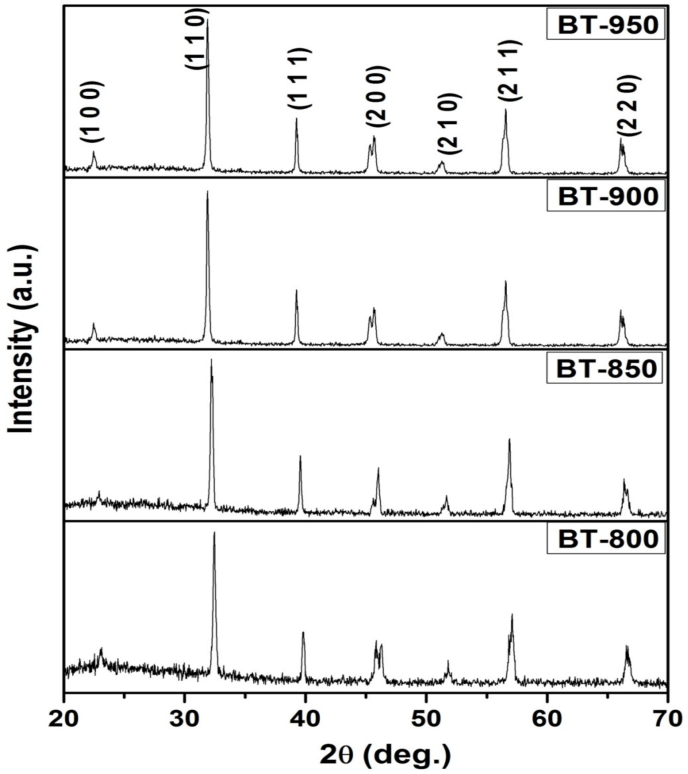

Figure 4. XRD patterns of $BaTiO_3$ sintered at different temperatures.

Table 1. Data of lattice parameters, X-ray density, bulk density, and porosity of sintered samples.

Sintering temperature (°C/30 min)	Lattice parameters a (Å)	c (Å)	X-ray density (d_x) (g/cm^3)	Bulk density (d_b) (g/cm^3)	Porosity (P) (%)
800	3.898	4.000	5.164	4.337	16
850	3.899	4.000	5.099	4.383	14
900	3.992	4.002	5.096	4.434	13
950	3.999	4.004	5.086	4.526	11

Figure 5 shows the SEM picture of the sintered $BaTiO_3$ samples. The microstructure properties such as grain size, grain distribution, porosity, presence of different phases, and interphases in these materials significantly influence the properties. It is therefore essential to have a detailed microstructure analysis of the sintered materials. It is clear from the photographs that the samples possess fine crystallites with dense microstructure. Table 2 gives the values of grain sizes at different sintering temperatures. As the sintering temperature increases, the average grain size also increases, and it was found to be in the range of 65 to 110 nm.

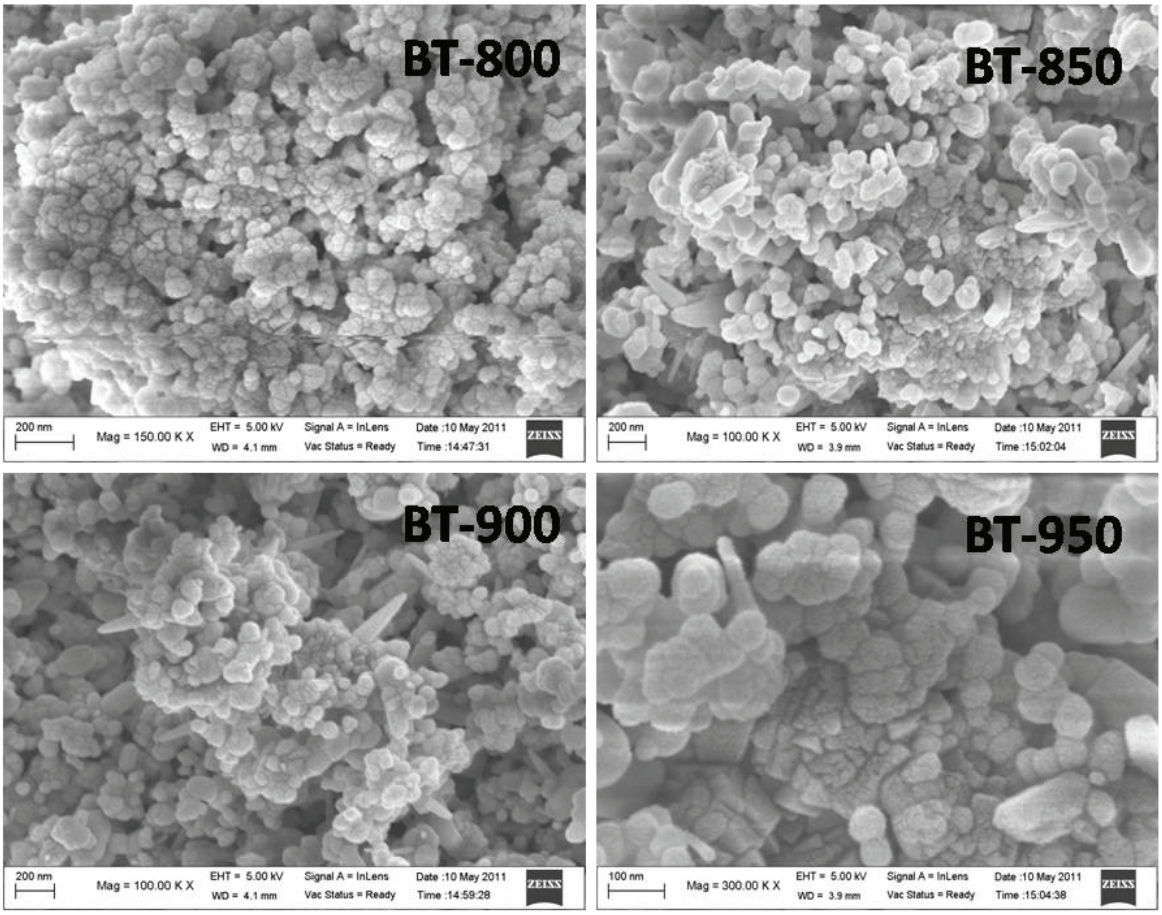

Figure 5. SEM images of the sintered $BaTiO_3$ samples.

Table 2. Data of grain size, ferroelectric properties, and dielectric properties.

Sintering temperature (°C/30 min)	Grain size (nm)	P_s ($\mu C/cm^2$)	E_c (kV/cm)	ε' tanδ	
800	65	—	15 63	0.006	
850	78	21	9	70	0.009
900	90	24	8	84	0.012
950	110	33	3	90	0.017

3.3. P-E measurements

Figure 6 shows the room temperature ferroelectric hysteresis loops of $BaTiO_3$ sintered at different temperatures. The sintered samples exhibit typical ferroelectric hysteresis, which indicates that they are spontaneously polarized. The ferroelectric hysteresis behavior gradually strengthens with an increase of sintering temperature. The values of polarization (P_s) and coercive field (E_c) (P_s and E_c taken from the positive intercept of the ferroelectric hysteresis loops at zero polarization) are given in Table 2. The polarization increases and the coercive field decreases with an increase of sintering temperature, which implies that the samples are becoming more easily polarized under the applied electric field. A gap exists in the P-E curves when the electric field becomes

zero. Another phenomenon is that the positive coercive field ($+E_c$), positive remnant polarization ($+P_r$), and their negative counter parts are asymmetric about the original point. According to Li et al., the uneven pinning of the domains in the samples contributes strongly to the asymmetry of the P-E loop [16]. Because the domain walls in ferroelectrics are relatively thin, they can be pinned by point (atomic) defects or charged species such as electrons, which may diffuse into charged domain walls [17–22]. Other pinning mechanisms are associated with the fields created inside grains by electrical [23] and/or elastic dipole defects [24]. Movement of domain walls can also be inhibited by imperfections at the grain boundaries, and dislocations, or could be related to the grain-size-induced internal stresses [25–27]. The tilt of the loops can be explained by the presence of a dielectric layer on the top of the ferroelectric material [28,29]. This layer, which has a lower dielectric constant than the ferroelectric material, separates the bound charges that are due to the ferroelectric polarization from the compensating charges on the electrodes. Because of the incompletely compensated polarization charge, a field, called the depolarizing field, will develop across the ferroelectric material, even if the top and bottom electrodes are shorted. The tilt of the loops can thus be taken as an indication of the presence of a low dielectric-constant ('passive') layer in series with the ferroelectric layer.

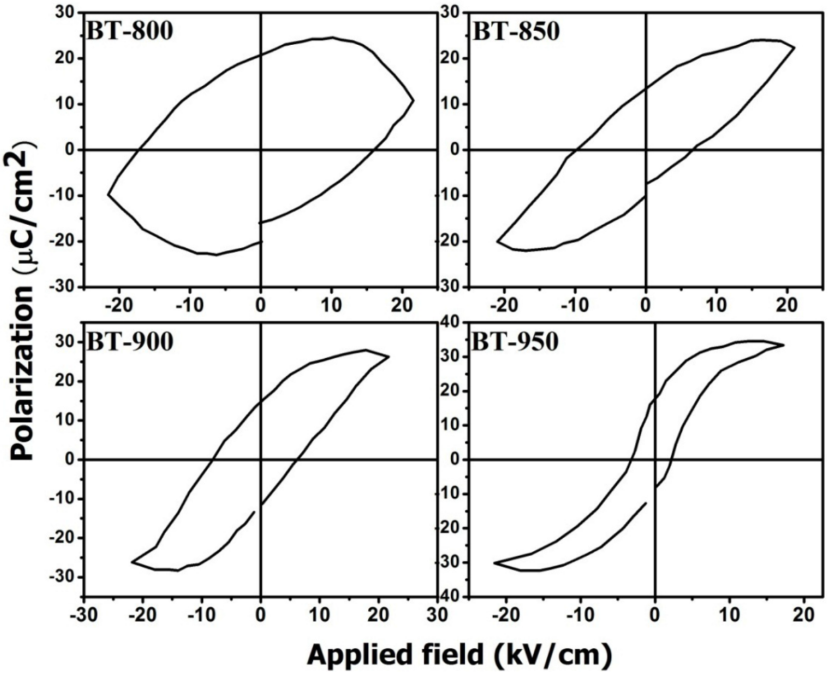

Figure 6. Ferroelectric hysteresis loops of $BaTiO_3$ samples.

3.4. Dielectric studies

3.4.1. As a function of frequency

Figures 7a and 7b give the frequency dependence of the dielectric constant (ε') and dielectric loss ($\tan\delta$) for all the samples in the range of 100 Hz to 1 MHz at room temperature, respectively. Table 2 gives the room temperature values of the dielectric constant and $\tan\delta$ at 1 MHz. It may be noted from Figure 7a that as the frequency increases, the values of the dielectric constant (ε') decrease and remain constant at higher frequencies, indicating dielectric dispersion. This may be attributed to the dipoles resulting from changes in valence states of cations and space-charge polarization [30]. It can be observed that the values of the dielectric constant increase

as the sintering temperature increases. The increase of dipoles leads to the increase of local displacements in the direction of the externally applied electric field for electrons, and the increased polarization causes a significant enhancement of the dielectric constant [31]. At higher frequencies, the dielectric constant remains independent of frequency due to the inability of the electric dipoles to follow the alternating applied electric field [32].

Figure 7b shows the frequency variation of dielectric loss ($\tan\delta$) for all the samples under investigation. It can be seen that the value of $\tan\delta$ increases at low frequencies and decreases at higher frequencies, which is similar to the results displayed in Figure 7a, as for hopping frequency equal to or nearly equal to that of the external applied field, the value of dielectric loss increases at a higher frequency. At low frequencies the value of $\tan\delta$ is considerably high due to the contribution of DC conductivity.

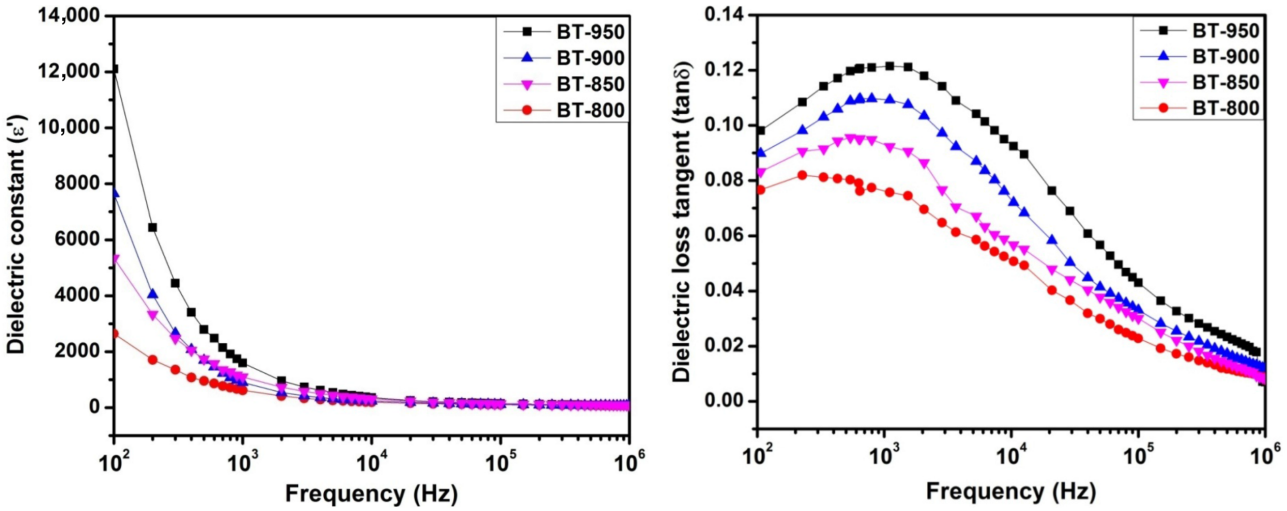

Figure 7. Frequency dependence of a) dielectric constant (ε') and b) dielectric loss ($\tan\delta$) at room temperature.

3.4.2. As a function of temperature

Figure 8 shows the temperature dependence of the dielectric constant (ε) of $BaTiO_3$ at 1 kHz for all samples under investigation. The dielectric constant increases with an increase of temperature up to Curie temperature (T_c) and then decreases. Since the charge hopping is a thermally activated process, dielectric polarization increases with increasing temperature, resulting in an increase of the dielectric constant. The dielectric constant (ε) of a material has 4 polarization contributions: electronic polarization (ε_e), ionic polarization (ε_i), dipolar polarization (ε_d), and space-charge polarization (ε_s). Response frequencies for electronic and ionic polarization are $\sim 10^{16}$ and 10^{13} Hz, respectively, and at frequencies above 100 kHz, contribution from space-charge polarization is not expected [33]. This saturation of space-charge polarization results in low dielectric constant values at higher frequencies. As frequency is increased, the dielectric constant is observed to decrease in all the samples, which is a normal behaviour of these materials [34], and at a frequency of 100 kHz, contribution from space-charge polarization is likely to be dominant [35]. The decrease in the dielectric constant is rapid at lower frequencies and becomes slower at higher frequencies. At the higher frequencies, the dipoles cannot follow the applied AC electric field, resulting in the decrease of the dielectric constant at higher frequencies. The high values of the dielectric constant at low frequencies can thus be attributed to the presence of such space charges in the samples. At lower frequencies, the dipolar and interfacial polarizations contribute significantly to the dielectric constant. Both of these are temperature-sensitive; hence, the dielectric constant increases at higher

rates for 1 kHz as compared to other frequencies (i.e. 10 kHz, 100 kHz, and 1 MHz not shown in Figure 8). At high frequencies only electronic polarization becomes significant, rather than dipolar.

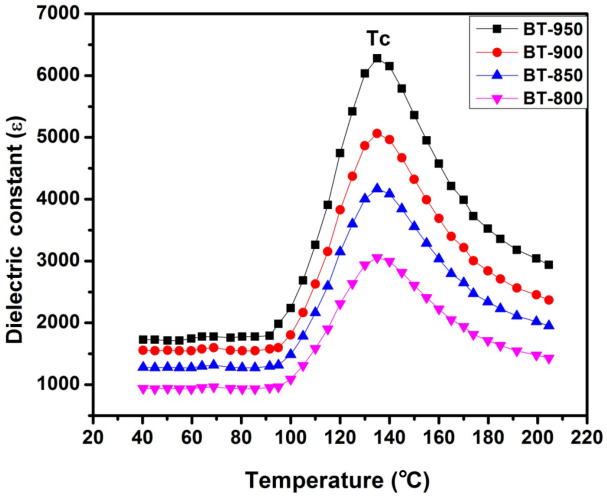

Figure 8. Temperature dependence of dielectric constant of $BaTiO_3$ at 1 kHz.

It can be observed from Figure 8 that the Curie temperature (T_c) for $BaTiO_3$ was nearly 137 °C at 1 kHz, which is slightly greater than in earlier reports [36]. This rise in T_c is attributed to the larger grain size (Table 2.) [37]. Hiroshima et al. [38] reported a close relation between the Curie temperature and internal stresses developed in the constrained grains at the phase transition temperature. The internal stress can shift the T_c to higher temperatures with increased grain size [39].

4. Conclusions

The nanopowders of $BaTiO_3$ were synthesized using the M-H method at 160 °C/45 min. The FTIR spectra of $BaTiO_3$ show 2 absorption bands in the ranges of 640–480 and 480–375 cm^{-1} due to the stretching vibration along the polar (c) axis and bending vibration of TiO_6 octahedra, respectively. No impurity phases were observed. Sintered XRD patterns showed formation of $BaTiO_3$. The lattice parameters were found to be increasing from 3.897 to 3.999 Å with sintering temperature. The grain sizes of all the samples were found to be in the range of 65 to 110 nm. The values of polarization and the coercive field of the sintered samples were found be increasing and decreasing with an increase of sintering temperature. The dielectric constants of the samples were increasing from 63 to 90 with increase of temperature.

Acknowledgments

One of the authors (K Praveena) is thankful to UGC, New Delhi, for the Dr DS Kothari Postdoctoral Fellowship.

References

[1] Guangneng, H. L.; Xueguang, H. *J. Cryst. Growth* **2005**, *279*, 489–549.

[2] Li, B.; Wang, X.; Li, L. *Mater. Chem. Phys.* **2002**, *78*, 292–298.

[3] Wang, X.; Lee, B. I.; Hu, M.; Payzant, E. A.; Blom, D. A. *J. Eur. Ceram. Soc.* **2006**, *26*, 2319–2326.

[4] Phule, P. P.; Risbud, S. H. J. Mater. Sci. 1990, 25, 1169–1183.

[5] Potdar, S. H.; Deshpande, S. B.; Date, S. K. *J. Amer. Ceram. Soc.* **1996**, *79*, 2795–2797.

[6] Shekar, M. A.; Dhanraj, G.; Bhat, H. L.; Patil, K. C. *J. Mater. Sci. Mater. Electron.* **1992**, *3*, 237.

[7] Phule, P. P.; Risbud, S. H. *Adv. Ceram. Mater.* **1988**, *3*, 183–185.

[8] Salze, H.; Odier, P.; Cales, B. *J. Non-Cryst. Solids* **1986**, *82*, 314–320.

[9] Kakihana, M.; Arima, M.; Nakamura, Y.; Yashima, M.; Yoshimura, M. Chem. Mater. 1999, 11, 438–450.

[10] Kutty, T. R. N.; Balachandran, R. Mater. Res. Bull. 1984, 19, 1479–1488.

[11] Sadhana, K.; Krishnaveni, T.; Praveena, K.; Bharadwaj, S.; Murthy, S. R. *Scrip. Materia* **2008**, *59*, 495–498.

[12] Metaxas, A. C.; Binner, J. G. P. *Advanced Ceramic Processing Technology*; Park Ridge, NJ, USA: Noyes Publishing, 1990.

[13] Komarneni, S.; Li, Q. H.; Roy, R. J. Mater. Chem. 1994, 4, 1903–1906.

[14] Smit, J.; Wijn, H. P. J. *Ferrites*; Eindhoven: Phillips Tech. Library, 1959.

[15] Qi, X.; Zhou, J.; Yue, Z.; Gui, Z.; Li, L.; Buddhudu, S. *Adv. Func. Mater.* **2004**, *14*, 920–926.

[16] Qi, X.; Zhou, J.; Yue, Z.; Gui, Z.; Li, L. *J. Magn. Magn. Mater.* **2004**, *269*, 352–358.

[17] Warren, W. L.; Dimos, D.; Tuttle, B. A.; Nasby, R. D.; Pike, G. E. Appl. Phys. Lett. 1994, 65, 1018–1020.

[18] Voigt, J. A.; Nasby, R. D. J. Appl. Phys. 1996, 79, 1013–1016.

[19] Warren, W. L.; Dimos, D.; Tuttle, B. A.; Smyth, D. M. *J. Am. Ceram. Soc.* **1994**, *77*, 2753–2757.

[20] Warren, W. L.; Dimos, D.; Pike, G. E.; Vanheusden, K.; Ramesh, R. Appl. Phys. Lett. 1995, 67, 1689–1691.

[21] Warren, W. L.; Pike, G. E.; Vanheusden, K.; Dimos, D.; Tuttle, B. A.; Robertson, J. J. Appl. Phys. 1996, 79, 9250–9257.

[22] Warren, W. L.; Vanheusden, K.; Dimos, D.; Pike, G. E.; Tuttle, B. A. J. Am. Ceram. Soc. 1996, 79, 536–538.

[23] Carl, K.; Haerdtl, K. H. *Ferroelectrics* **1977**, *17*, 473–486.

[24] Sagalowicz, L.; Chu, F.; Duran Martin, P.; Damjanovic, D. *J. Appl. Phys.* **2000**, *88*, 7258–7263.

[25] Arlt, G.; Pertsev, N. A. *J. Appl. Phys.* **1991**, *70*, 2283–2289.

[26] Buessem, W. R.; Cross, L. E.; Goswami, A. K. *J. Am. Ceram. Soc.* **1992**, *75*, 2923–2926.

[27] Demartin, M.; Damjanovic, D. Appl. Phys. Lett. 1996, 68, 3046–3049.

[28] Tagantsev, A. K.; Landivar, M.; Colla, E.; Setter, N. *J. Appl. Phys.* **1995**, *78*, 2623–2630.

[29] Robels, U.; Calderwood, J. H.; Arlt, G. J. Appl. Phys. 1995, 77, 4002–4008.

[30] Devan, R. S.; Chougule, B. K. J App. Phys. 2007, 101, 014109-6.

[31] Eihiti, M. A. *J. Magn. Magn. Mater.* **1996**, *164*, 187–196.

[32] Patankar, K. K.; Dombale, P. D.; Mathe, V. L.; Patil, S. A.; Patil, R. N. *Mater. Sci. Eng. B* **2001**, *8*, 53.

[33] Buchanan, R. C. *Ceramic Materials for Electronic Processing: Properties and Applications*; New York: Marcel Dekker Inc., 1986.

[34] Lines, M. E.; Glass, A. M. *Principles and Applications of Ferroelectric and Related Materials*; Oxford: Clarendon Press, 2001.

[35] Rukmini, H. R.; Choudhary, R. N. P.; Prabhakara, D. L. *Mater. Chem. Phys.* **2000**, *64*, 171–178.

[36] Paletto, J.; Grenge, G.; Goutte, R.; Eyraud, L. J. Phys. D Appl. Phys. 1974, 7, 78–84.

[37] Hwang, H. J.; Nagai, T.; Ohji, T.; Sando, M. *J. Am. Ceram. Soc.* **1998**, *81*, 709–712.

[38] Hiroshima, T.; Tanaka, K.; Kimurra, T. *J. Am. Ceram. Soc.* **1996**, *79*, 3235–3242.

[39] Arlt, G.; Hennings, D.; de With, G. J. Appl. Phys. 1985, 58, 1619.